USGS
science for a changing world

Three-Dimensional Geologic Map of the Brady Geothermal Area, Nevada

By Drew L. Siler, James E. Faulds, Nicholas H. Hinz, and John H. Queen

Pamphlet to accompany
Scientific Investigations Map 3469

2021

U.S. Department of the Interior
U.S. Geological Survey

U.S. Geological Survey, Reston, Virginia: 2021

Suggested citation:
Siler, D.L., Faulds, J.E., Hinz, N.H., and Queen, J.H., 2021, Three-dimensional geologic map of the Brady geothermal area, Nevada: U.S. Geological Survey Scientific Investigations Map 3469, 2 sheets, pamphlet 20 p., https://doi.org/10.3133/sim3469.

ISSN 2329–132X (online)

Contents

Figures

Map Sheets

1. Three-Dimensional Geologic Map of the Brady Geothermal Area, Nevada
2. Three-Dimensional Views of Structural Factors and Geothermal Production Wells at Brady Geothermal Area, Nevada

Three-Dimensional Geologic Map of the Brady Geothermal Area, Nevada

By Drew L. Siler,[1] James E. Faulds,[2] Nicholas H. Hinz,[3] and John H. Queen[4]

Abstract

The three-dimensional (3D) geologic map characterizes the subsurface in the Brady geothermal area in the northern Hot Springs Mountains of northwestern Nevada. We built the 3D map by integrating the results from detailed geologic mapping, seismic-reflection, potential-field-geophysical, and lithologic well-logging investigations completed in the study area. This effort was undertaken to investigate the geologic structure in the geothermal field and geologic controls on hydrothermal circulation. This characterization of the controls on hydrothermal circulation is applicable to the assessment, exploration, and development of analogous geothermal resources. The 3D map area is 4 kilometers (km) wide along the west-northwest-to-east-southeast axis and 6 km wide along the north-northeast-to-south-southwest axis and extends to 1.0 km below sea level, approximately 2.5 km below the land surface. We describe the geologic units and structures in the map area, discuss the methods used to integrate the geologic and geophysical information into the 3D geologic interpretation, and calculate several geologic factors that may aid in our understanding of hydrothermal circulation. Map sheet 1 provides horizontal and vertical section views and oblique perspective views from several angles of the 3D geologic map. Map sheet 2 provides views of derivative calculations based on the 3D geologic data, 3D density of faults, 3D density of fault intersections and terminations, slip tendency on 3D faults, and dilation tendency on 3D faults. We provide digital data for all elements of the map, such as individual 3D fault and stratigraphic surfaces, 3D fault density, 3D fault intersection density, 3D slip tendency on fault surfaces, and 3D dilation tendency on fault surfaces. A brief movie displaying the 3D map is available at https://doi.org/10.3133/sim3469.

Purpose and Scope

The purpose of the three-dimensional (3D) Brady geothermal area map is to describe the fault system and the lithologic section in the Brady geothermal area in the context of elucidating the geologic controls on hydrothermal circulation. The Brady geothermal area is located in the northern Hot Springs Mountains, approximately 40 kilometers (km) north-northwest of the city of Fallon, Nevada, and 30 km northeast of the city of Fernley, Nevada (fig. 1). The Brady geothermal area has been the subject of many academic studies (Benoit and others, 1982; Faulds and others, 2003, 2010a,b, 2017; Kratt and others, 2006; Jolie and others, 2015; Ali and others, 2016; Patterson and others, 2017; Cardiff and others, 2018; Li and Zhan, 2018; Parker and others, 2018; Reinisch and others, 2018, and those cited herein) and thus there is a wealth of data in the public domain. The detailed subsurface structure and the specific geologic controls on geothermal processes at Brady have been inferred through assessment of the structural setting (Faulds and others, 2010a,b) and integration of detailed geologic mapping with geophysical data and well logs (Faulds and others, 2017). An initial 3D model for the area was generated by Jolie and others (2015). However, some aspects of the controls on geothermal activity have remained elusive. This 3D geologic map provides additional characterization of the subsurface to better understand the controls on hydrothermal production in the area. This 3D map consists of this pamphlet and two map sheets. Map sheet 1 shows the 3D geologic map, and map sheet 2 shows the spatial relations between the geothermal production wells at Brady and four structural characteristics that may control the distribution of fluid flow pathways in the subsurface.

Introduction

The 3D geologic map and this report describe the subsurface geology and structure of part of the northern Hot Springs Mountains including the Brady geothermal area, western Nevada (figs. 1 and 2). Geology and geothermal processes in the Brady area have been studied since 1959, with geothermal-derived electricity produced at Brady since 1992 (Benoit and Butler, 1983). Geothermal fluids are produced from two different

[1]U.S. Geological Survey.

[2]Nevada Bureau of Mines and Geology.

[3]Geologica Geothermal Group, Inc.

[4]Hi-Q Geophysical, Inc.

reservoir levels in the subsurface: 650 meters (m) depth (600 m elevation) and 1,700 m depth (−450 m elevation). The geothermal system supplies heat to two power stations and to a direct-use vegetable dehydration facility. Electricity production capacity from the power stations is 26.1 megawatts electrical (MWe), and ~7 megawatts thermal (MWth) is supplied to the drying facility. The 3D map spans a 6 km (south-southwest-to-north-northeast) by 4 km (west-northwest-to-east-southeast) area (24 square kilometers [km^2]) that extends from the surface (approximately 1,218–1,515 m elevation) to 1.0 km below sea level. The geologic

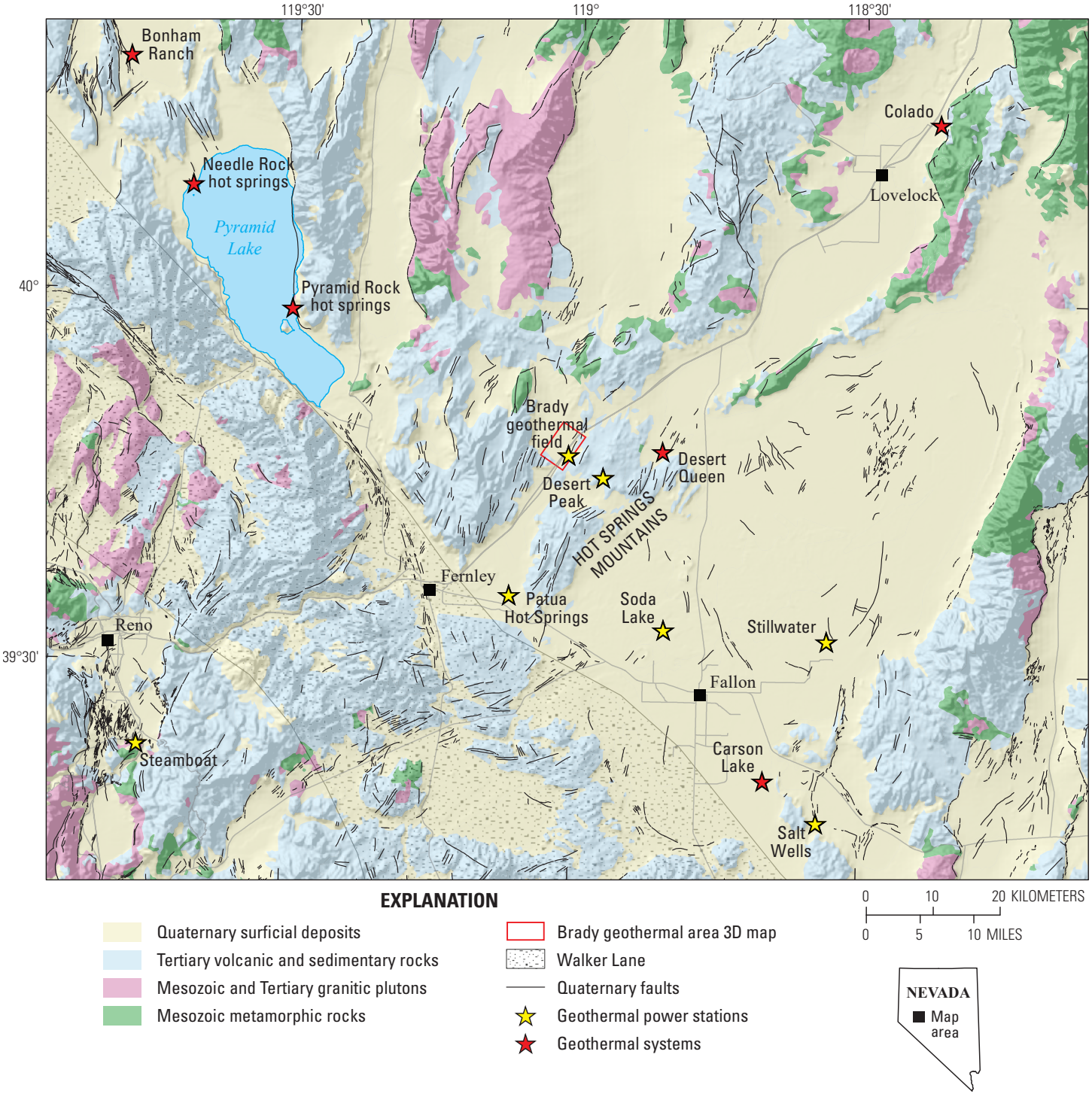

Figure 1. Regional geologic map of the region surrounding the northern Hot Springs Mountains showing generalized geology (Crafford, 2010) and the location of the Brady geothermal area three-dimensional (3D) map. Geothermal systems shown have operating power stations or measured or estimated temperatures greater than 150 degrees Celsius (°C) (Faulds and others, 2006, 2011). Quaternary faults from Crafford (2007) and U.S. Geological Survey Quaternary fault and fold database (U.S. Geological Survey, 2006). Shaded relief from U.S. Geological Survey National Geospatial Program, available at https://www.usgs.gov/core-science-systems/national-geospatial-program/national-map.

relations shown in the 3D map are based on interpretations of geologic and geophysical data, as well as subsequent construction of 3D geologic surfaces (faults and geologic contacts) using 3D interpolation algorithms. The resulting 3D geologic map displays subsurface fault surfaces, stratigraphic contacts, and rock volumes.

Definition of the geologic and structural features of the 3D map is supported by two-dimensional (2D) geologic cross sections (fig. 3) that fully integrate the well and geophysical data (Faulds and others, 2017), lithologic analyses of about 19,000 m of cores and cuttings from 21 wells located within the mapped area (figs. 4 and 5), analyses of structural features and fluid-flow zones in 20 wells within the 3D map (fig. 6), data from seismic reflection interpretation (fig. 7), interpretation of gravity anomalies and horizontal gravity gradients (fig. 8), and 3D gravity inversion modeling (Witter and others, 2016). Potential applications of this map include (1) reservoir modeling and management of the geothermal reservoir, (2) seismicity hazard analysis, (3) conventional geothermal and enhanced geothermal system research and exploration, (4) education and scientific inquiry, and (5) basin hydrogeology (see Potential Applications for 3D Map section of this report).

Geologic Setting

Several tectonic episodes have affected the region surrounding the northern Hot Springs Mountains since the Mesozoic. Geologic features representative of these episodes are expressed in the 3D map. The oldest tectonism expressed in the Brady area is Mesozoic contractional deformation, including arc and back-arc volcanism and sedimentation, low-grade metamorphism, folding and thrusting of the Mesozoic section, and uplift and erosion (for example, Schweickert and Cowan, 1975; Stewart and Carlson, 1978; Oldow, 1984). Following Mesozoic tectonism, in the Oligocene to early Miocene, regionally extensive ash-flow tuff sequences were erupted and deposited across the paleo-topography that had developed on the uplifted and deformed Mesozoic and older rocks (Henry, 2008; Henry and others, 2012). Subsequently throughout the Miocene, regionally extensive and dominantly mafic lava flows and domes associated with the ancestral Cascade volcanic arc were erupted on the Oligocene section. This Miocene mafic volcanism included back-arc rifting and development of local sedimentary basins (Wernicke and others, 1987; Cousens and others, 2008). Contemporaneous with the Miocene mafic volcanism, east-west to west-northwest Basin and Range extension commenced throughout western Nevada in the early to middle Miocene. This extension, which continues to the present, is accommodated along steeply dipping, generally north-northeast-striking normal faults in the region (Stockli and others, 2002; Colgan and others, 2006; Fosdick and Colgan, 2008). Along with normal faulting, Basin-and-Range-style deformation included the development of extensional folds and a variety of structural features including fault stepovers or relay ramps (for example, Faulds and Varga, 1998). Although not expressed in the Brady geothermal area, Walker-Lane-type dextral faulting began in northwestern Nevada in the late Miocene and is certainly evident within about 20 km of the Brady area (Cashman and Fontaine, 2000; Faulds and others, 2005; fig. 1). As a result of high regional heat flow associated with regional crustal thinning and local permeability associated with active Basin-and-Range-type and Walker-Lane-type faulting in Miocene to recent time, geothermal circulation cells developed along many fault systems in western Nevada (Blackwell and others, 1999; Faulds and others, 2006, 2011).

The major fault systems across the northern Hot Springs Mountains and map area are predominantly north-northeast striking and northwest dipping, though several southeast-dipping faults are present as well. The youngest faults in the 3D map, which include the Brady fault zone (fig. 2), cut approximately 15.5-thousand-year-old (ka) lacustrine sediments (Faulds and others, 2017). Paleoseismic trenching along the Brady fault and within the map area (fig. 2) has identified at least one slip event with approximately 2 m vertical displacement since about 15.5 ka (Wesnousky and others, 2005).

The stratigraphic section in the Brady area predominantly dips to the southeast in fault blocks that have been tilted and down-dropped along northwest-dipping normal faults. The southeast-dipping section is part of a series of extensional folds (for example, Faulds and Varga, 1998) extending across the northern Hot Springs Mountains associated with alternating southeast-dipping faults with west-dipping strata and northwest-dipping faults with east-dipping strata (Faulds and others, 2010a, 2012, 2017).

Data

Well Cuttings, Cores, and Other Data

Lithologic data from 21 wells within the 3D map volume are used to constrain stratigraphic and structural relations. For 20 of these wells, well cuttings were analyzed. For two wells (BCH-3 and BCH-2) core was analyzed. Core was evaluated by hand lens whereas cuttings were examined under a high-power binocular microscope. Both cuttings and core provide reliable stratigraphic control, with the caveat that the precision in the depth of stratigraphic contacts identified from cuttings is likely no greater than about 10 m, since cuttings are typically sampled every 9.1 meters (30 feet) during drilling. Petrographic thin sections at varying intervals were made for several wells and used in tandem with the core and cuttings to confirm lithologic interpretations and provide additional detail on composition. Based on these analyses, contacts between lithologic units were picked (fig. 5). Lithologic logs from mud logs were not used in this analysis, because they can vary in quality and reliability.

The analyses of core and cuttings also included documentation of any evidence for faulting in the 21 wells that have lithologic data. Evidence for faulting that was documented includes slickensides, druse or euhedral secondary mineralization such as quartz or calcite, or clay gouge, though clay gouge is rarely preserved in cuttings. For 20 additional wells, well completion reports, mud logs, or other logs were available that indicated the location of fractured zones, loss circulation zones,

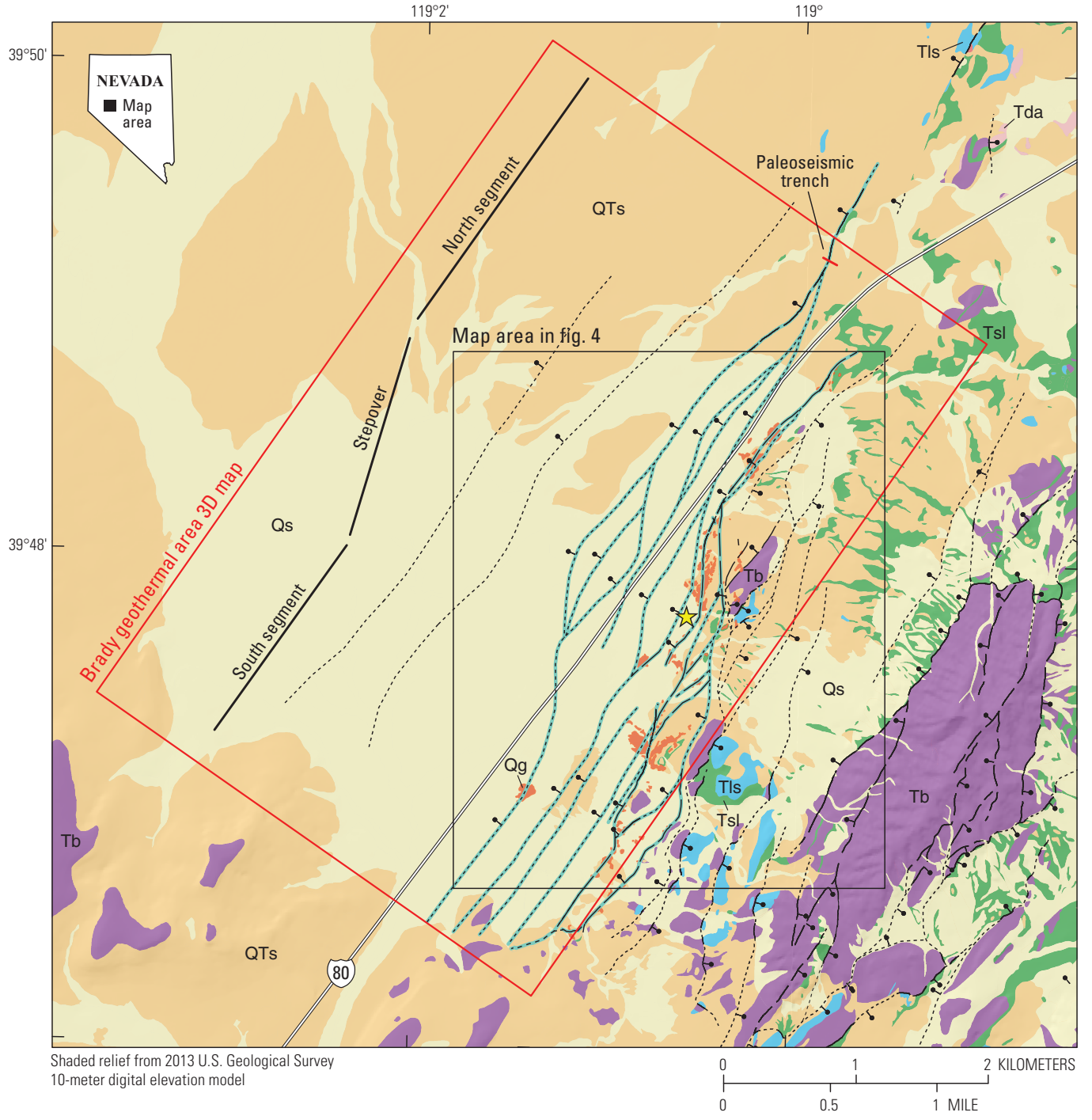

EXPLANATION

- Qg — Geothermal deposits and features (Holocene to late Pleistocene)
- Qs — Surficial sediments and sedimentary rocks (Holocene to late Pleistocene)
- QTs — Sedimentary rocks (late Pleistocene to late Miocene)
- Tsl — Lacustrine sedimentary rocks (late Miocene)
- Tls — Limestone (late Miocene)
- Tb — Basaltic lavas (late Miocene)
- Tda — Dacite and andesite lavas (early to middle Miocene)
- Brady fault zone
- Fault—Bar and ball on down-thrown block. Solid where certain; dashed where approximately located; dotted where concealed
- Brady geothermal power station

Figure 2. Geologic map of the Brady geothermal area. Geologic units are lumped from Faulds and others (2012, 2017). Red rectangle denotes the three-dimensional (3D) geologic map area. Location of the paleoseismic trench of Wesnousky and others (2005) is shown. The fault strands that compose the Brady fault zone are highlighted in teal.

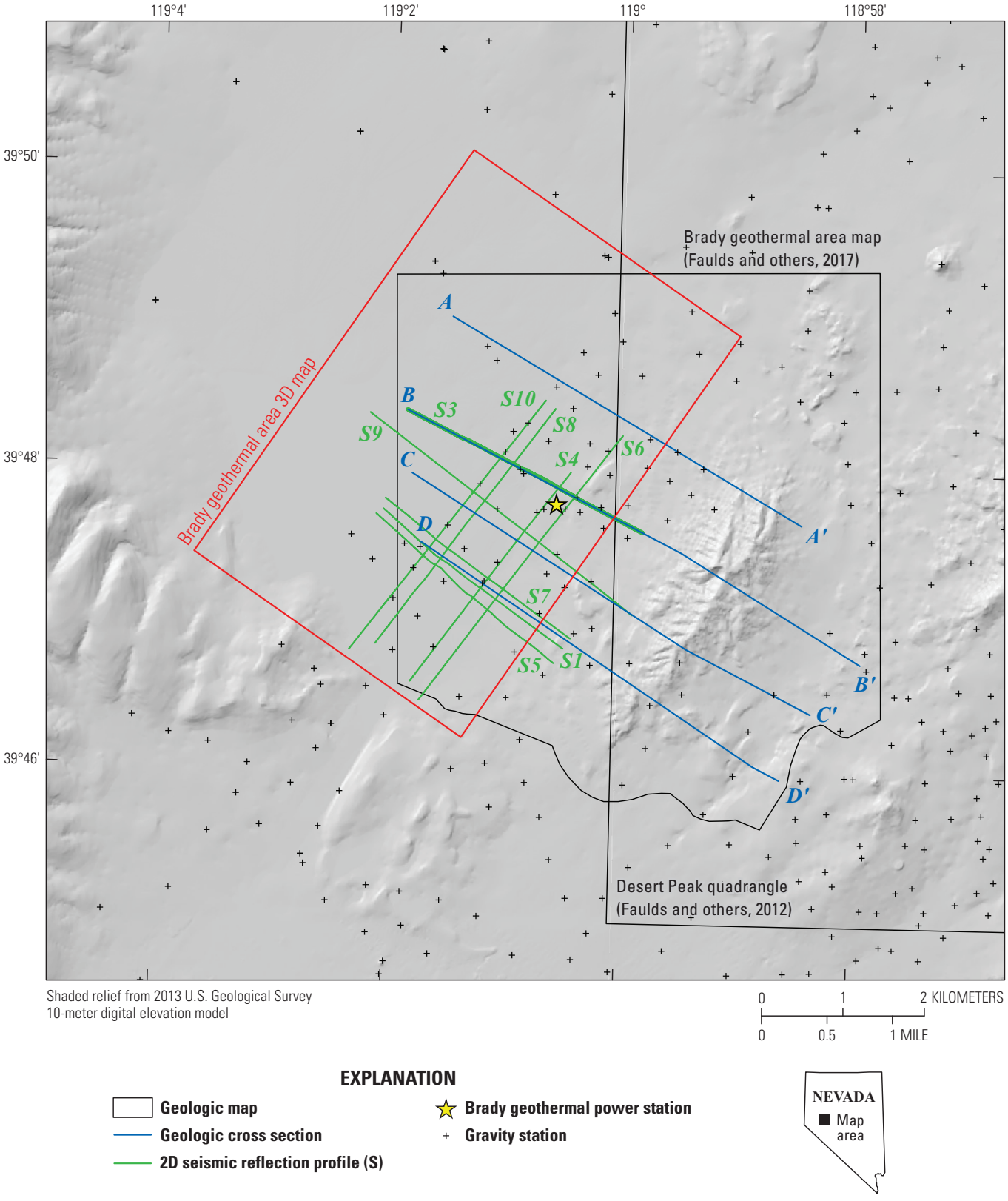

Figure 3. Shaded-relief map showing the location of data supporting the three-dimensional (3D) geologic map, including gravity data, two-dimensional (2D) seismic reflection profiles (Queen and others 2016), 2D geologic cross sections (Faulds and others, 2017), and geologic maps (Faulds and others, 2012, 2017).

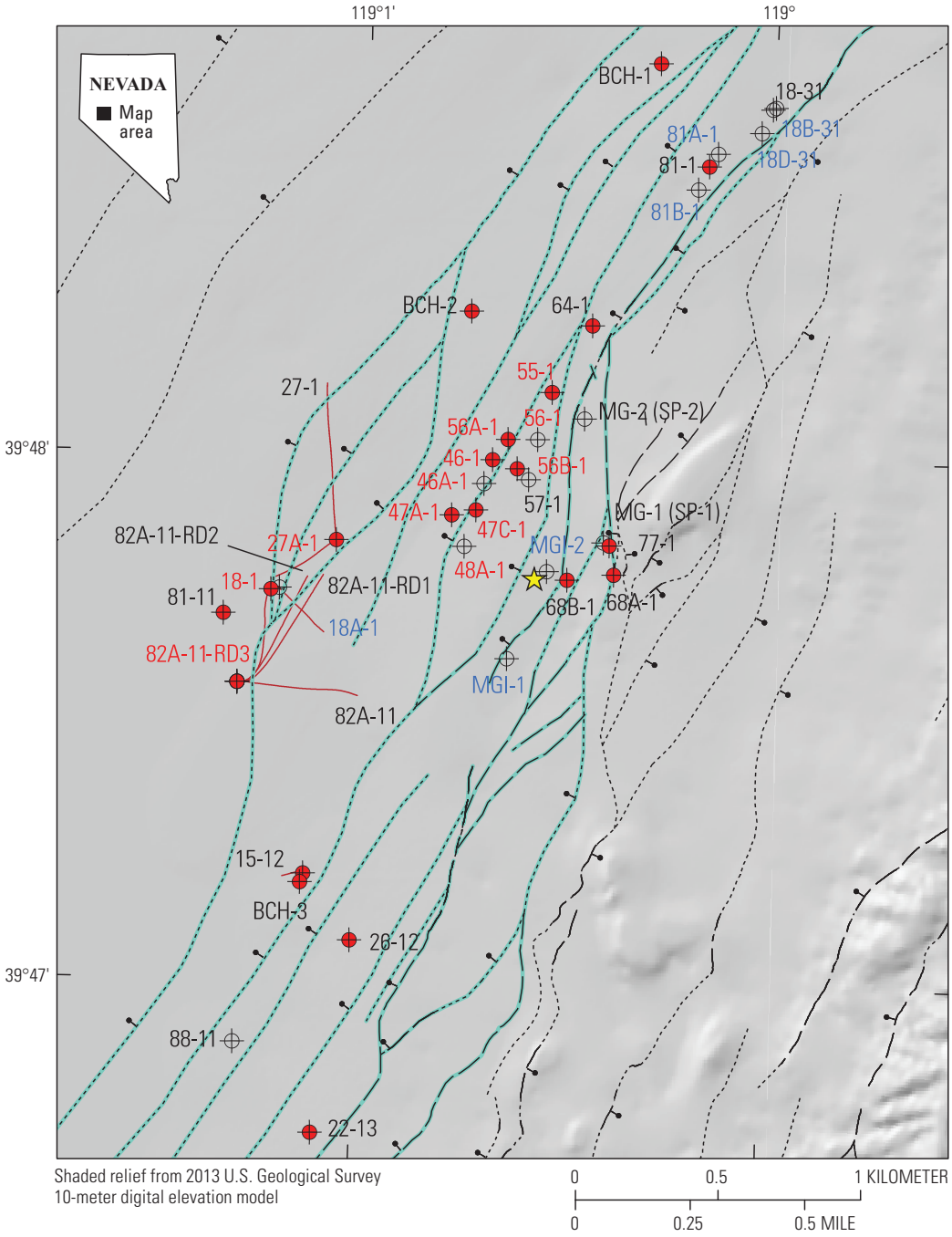

EXPLANATION

Brady fault zone

Fault—Bar and ball on down-thrown block. Solid where certain; dashed where approximately located; dotted where concealed

Wells—Red labels show production wells, blue labels show injection wells, and black labels show other wells

Wells with lithologic logs (fig. 5)

Wells without lithologic logs (fig. 6)

Well paths for non-vertical wells

Brady geothermal power station

Figure 4. Shaded-relief map of wells that have data supporting the three-dimensional (3D) geologic map. Map area shown on figures 2 and 3. The fault strands interpreted to form the Brady fault zone are highlighted in teal.

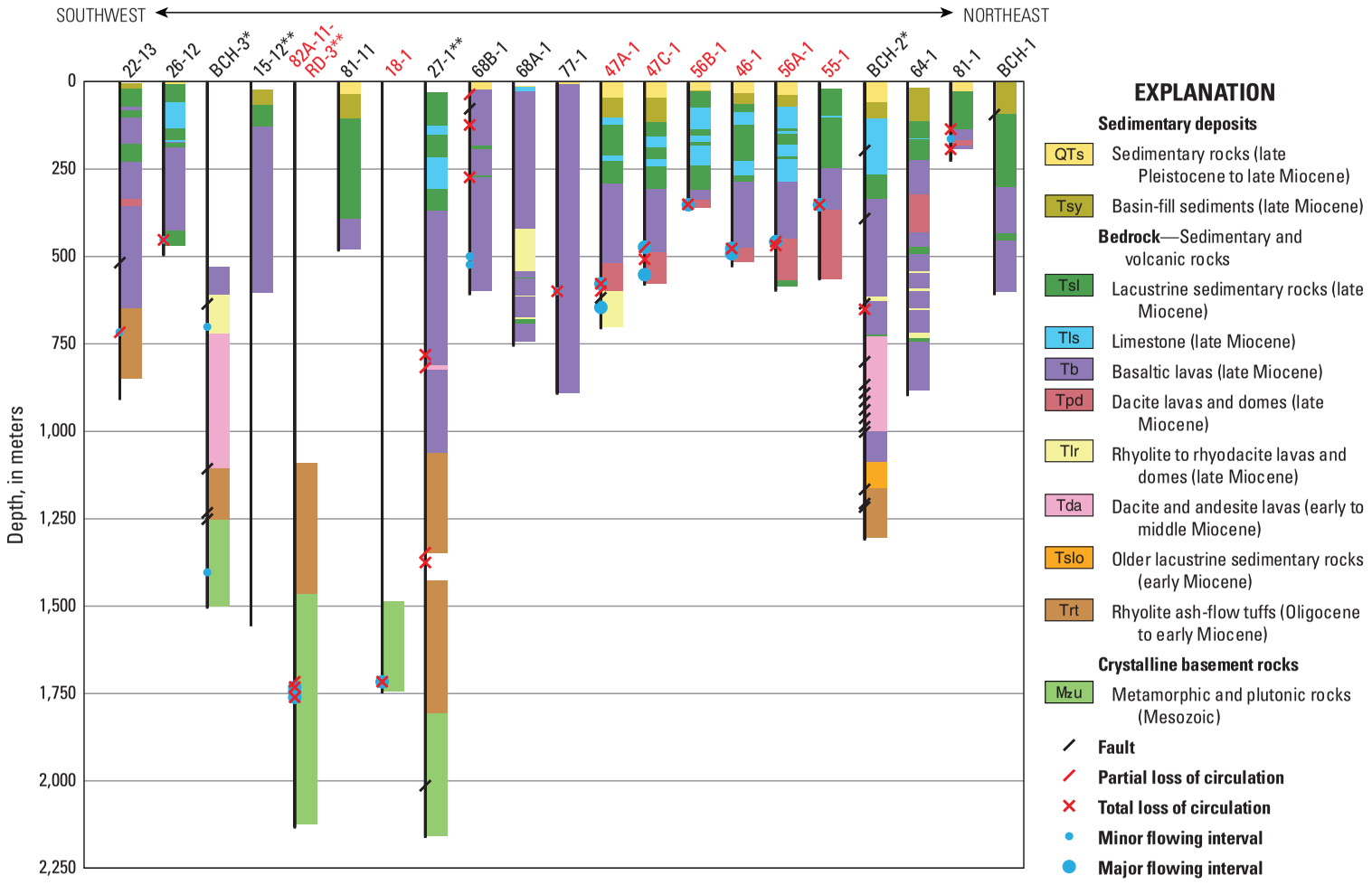

Figure 5. Lithologic logs and evidence for faulting, loss of circulation, or fluid flow from 21 wells in the Brady geothermal area for which cores or well cuttings were analyzed (locations shown in fig. 4). All wells are shown vertical in measured depth (rather than true vertical depth). Well names in red refer to wells that have been used for geothermal production. Well names in black refer to other wells. Cuttings or core were either unavailable or not analyzed for locations where no lithologic data are shown. A single asterisk (*) denotes wells for which core was analyzed and two asterisks (**) denote non-vertical wells (see fig. 4). Note that geothermal deposits (unit Qg) was not picked from well cuttings or core (it is identified by geologic mapping [Faulds and others, 2012, 2017]). Additionally, surficial sediments and sedimentary rocks (unit Qs) is very thin (<10 meters) throughout the map, so neither unit Qg nor Qs is shown on this figure.

and (or) flowing zones, all of which may be associated with fault zones (fig. 6). For wells that have been used for either production or injection of geothermal fluids at the Brady geothermal power station, publicly available production and injection reports denote the specific production or injection zone. On figures 5 and 6, production or injection zones are classified as major flowing zones. Other flowing zones are classified as minor flowing zones (figs. 5 and 6). These locations may also be associated with faults. Typically, loss zones and flowing zones (major and minor) correlate with evidence for faulting, though not always (figs. 5 and 6). Evidence for faults from the well data was interpreted alongside evidence for faults from stratigraphic, geophysical, and surficial geologic data. Typically, more than one piece of evidence was required to interpret a fault in a given location.

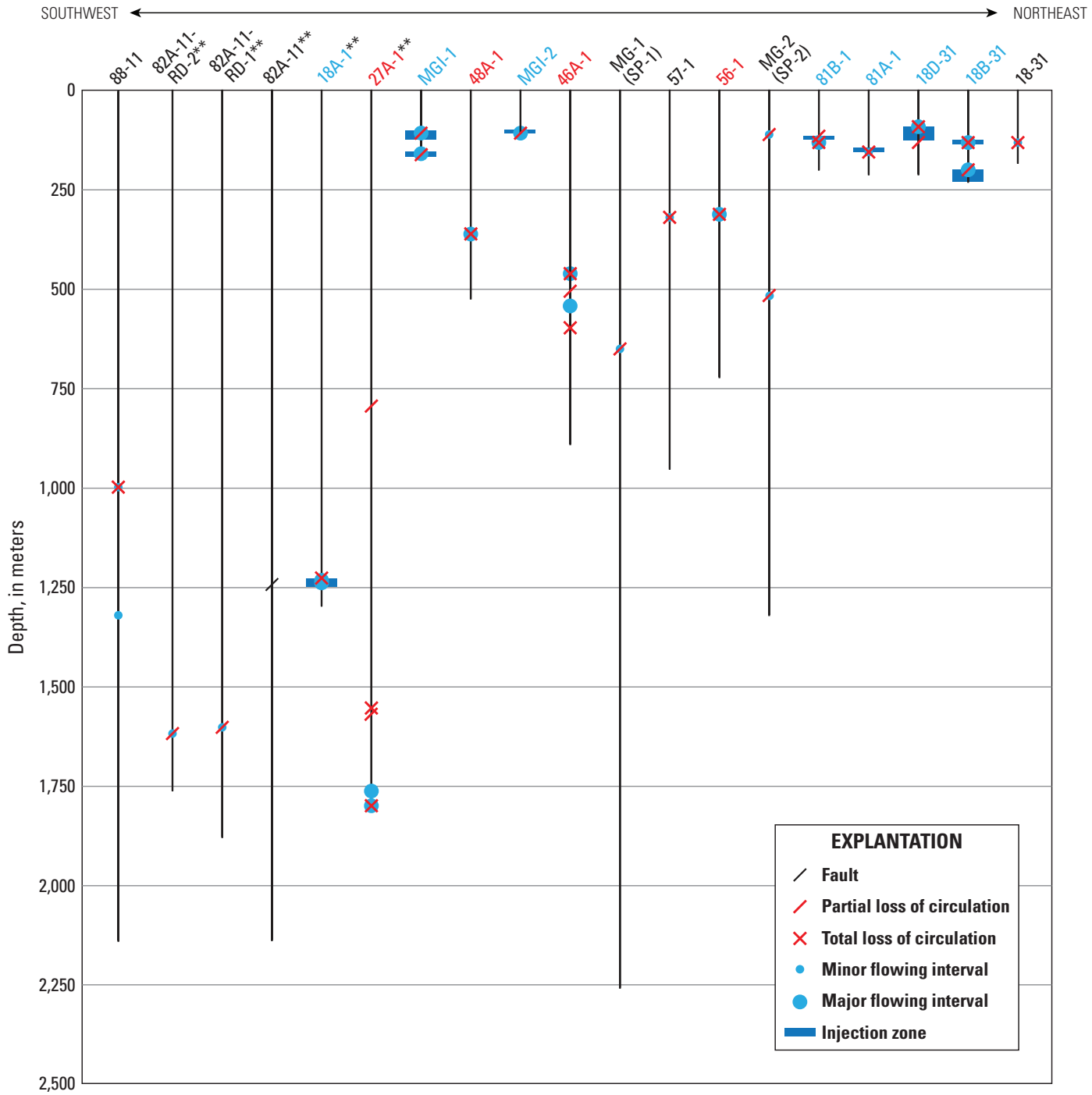

Figure 6. Evidence for faulting, loss of circulation, and fluid flow in 20 wells in the Brady geothermal area for which no cores or cuttings were analyzed (locations shown in fig. 4). All wells are shown vertical in measured depth (rather than true vertical depth). Well names in red refer to wells that have been used for geothermal production, well names in blue refer to wells that have been used for geothermal injection. Well names in black refer to other wells. Two asterisks (**) denote non-vertical wells; see figure 4.

Seismic Reflection Data

This study incorporated results from a 2D seismic reflection study (Queen and others, 2016). The locations of the seismic reflection profiles are shown in figure 3. As an example of the data and interpretation, line S3 (fig. 3) is shown both uninterpreted and interpreted along cross section *B*–*B*′ in figure 7. For details about the acquisition and processing of the data, the reader is directed to Queen and others (2016). A total of nine seismic reflection lines were interpreted and incorporated into the 3D map. The seismic reflection profiles show coherent reflections in the valley fill (units Qs, QTs, and Tsy), above the top of the Miocene mafic volcanic rocks (unit Tb). Below the top of unit Tb, high acoustic attenuation owing to the relatively thick volcanic section and (or) low impedance contrasts within the Cenozoic volcanic section result in relatively poor reflector coherence. Additionally, complex seismic velocity structure in the highly faulted area local to the geothermal field limits reflector coherence and therefore hinders confident interpretation of structural and stratigraphic relations in this area. Still, lateral reflector terminations in the basin-fill sediments (units Qs, QTs, and Tsy) proved useful in identification of faults that are not exposed at the surface (fig. 7).

Gravity Data

A publicly available database of approximately 6,700 gravity stations spanning the northern Hot Springs Mountains was analyzed to help constrain the 3D geometries of geologic contacts and faults in the 3D map volume (fig. 8). These data include published efforts described by Faulds and others (2010a, 2003) and Witter and others (2016). The 6- by 4-km area of the 3D map contains 53 gravity stations. Station spacing varies between about 250 and 500 m in the 3D map though is non-uniform throughout the study area. For instance, the data-free area in the western part of the map on figure 8 denotes that this area is 2 km or more from any gravity stations. The gravity interpretation is more uncertain in such data-sparse parts of the study area than it is in more data-rich parts. The remaining approximately 6,650 gravity stations are spaced at 100–1,600 m intervals throughout the approximately 125- by 125-km region surrounding the study area. The gravity data were collected and processed using methods detailed by Witter and others (2016), including description of data collection and processing. The complete Bouguer anomaly (CBA) was calculated using a density of 2.5 grams per cubic centimeter (g/cm^3) (Witter and others, 2016). The CBA reveals the general shape, size, and extent of the Hot Springs Flat basin adjacent to the Brady geothermal area. The maximum horizontal gradients were calculated using methods of Blakely (1995). These maxima define the most prevalent lateral changes in the gravity field and are typically caused by juxtaposition of geologic units that have different densities as a result of faulting.

Geologic Cross Sections

The seismic reflection interpretation (fig. 7), geologic maps (Faulds and others, 2012; 2017), downhole lithologic data, evidence for faulting along wells (figs. 5 and 6), and gravity data (fig. 8) were integrated into four geologic cross sections by Faulds and others (2017; cross section lines shown on fig. 3). In construction of the cross sections, downhole lithologic data within 500 m are projected to cross-section profiles. This cutoff represents the distance from cross-section profiles beyond which well data are expected to be of little or no use in constraining geology and structure owing to the closely spaced faults in the area. Lithologic data are simplified and lumped into stratigraphic units that represent the succession of units as identified from the cores and cuttings. Faults mapped at the surface are projected down dip based on their measured or inferred dip from geologic mapping and (or) seismic reflection interpretation. Downhole data projected to the cross sections help to constrain fault dip in the subsurface. Faults interpreted from the seismic reflection profiles, but not exposed at the surface were projected to the surface as concealed faults for the 2D map and included on the cross sections.

3D Geologic Mapping Methods

The Brady geothermal area 3D map was constructed using the methods summarized below, which are similar to other recent contributions (Moeck and others, 2010; Faulds and others, 2010b; Jolie and others, 2012, 2015; Hinz and others, 2013; Siler and Faulds, 2013; Siler and others, 2016a,b, 2019a,b). A previous 3D geologic map of the Brady geothermal area was produced by Jolie and others (2015). The 3D geologic map presented herein was re-built subsequent to this initial effort, incorporates new data, and adds significant structural and stratigraphic complexity. Commercially available software (EarthVision) was used for all 3D analysis.

The 3D fault architecture is initially built based on four geologic cross sections that span the 3D map (Faulds and others, 2017). As explained above, the cross sections are built by synthesizing faults interpreted from seismic reflection (Queen and others, 2016; fig. 7), 1:12,000-scale fault mapping (Faulds and others, 2017), faults interpreted from gravity anomalies and gravity horizontal gradients (fig. 8), faults inferred from cuttings and (or) cores, and faults inferred from losses of circulation, flow zones, or injection zones in wells. A fault hierarchy is constructed that defines the relative cross-cutting relations between faults—in other words, which faults terminate against other faults.

In evolving the fault architecture from the cross sections to three dimensions, there are unavoidable fault geometry and fault hierarchy inconsistencies that translate poorly to three dimensions. The projection of well data within 500 m to the cross sections, for instance, though necessary for cross-section construction, may result in unrealistic fault geometries and relations when the 3D faults are built. As a result, the cross sections, seismic reflection data, 2D geologic map, gravity data, and well data are reexamined. The initial 3D fault architecture and hierarchy is adjusted to ensure that the fault architecture is consistent with all the input data. Our integration of multiple datasets (geologic mapping, downhole data, seismic reflection, and gravity) into the fault interpretation helps to reduce the uncertainty associated with a particular dataset. For instance, as

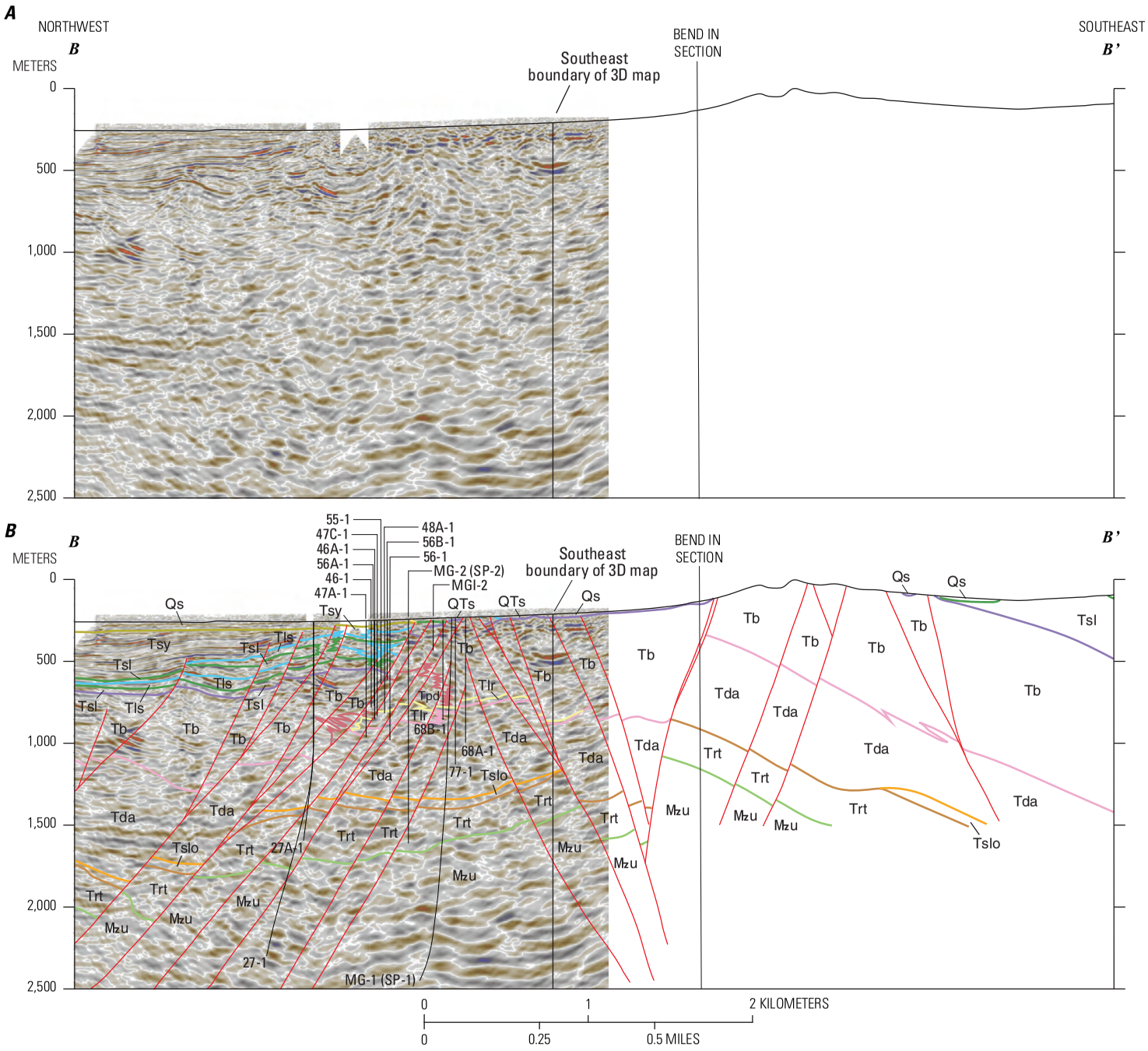

Figure 7. Seismic reflection data (*A*) and interpretation (*B*) of line S3 (profile ***B–B'*** in fig. 3). Seismic reflection data are only available for the left half of the profile. The interpreted geologic information shown in part *B* is adapted from Faulds and others (2017). The interpretation incorporates the seismic reflection data, analysis of gravity grids and horizontal gradients (fig. 8), geologic map data (fig. 2), and well data (figs. 4–6). Note that geothermal deposits (unit Qg) were not identified from seismic reflection (they are identified by geologic mapping [Faulds and others, 2012, 2017]), so unit Qg is not shown on this figure. Depths shown are below the seismic datum at 1,400 meters above sea level. 3D, three dimensional.

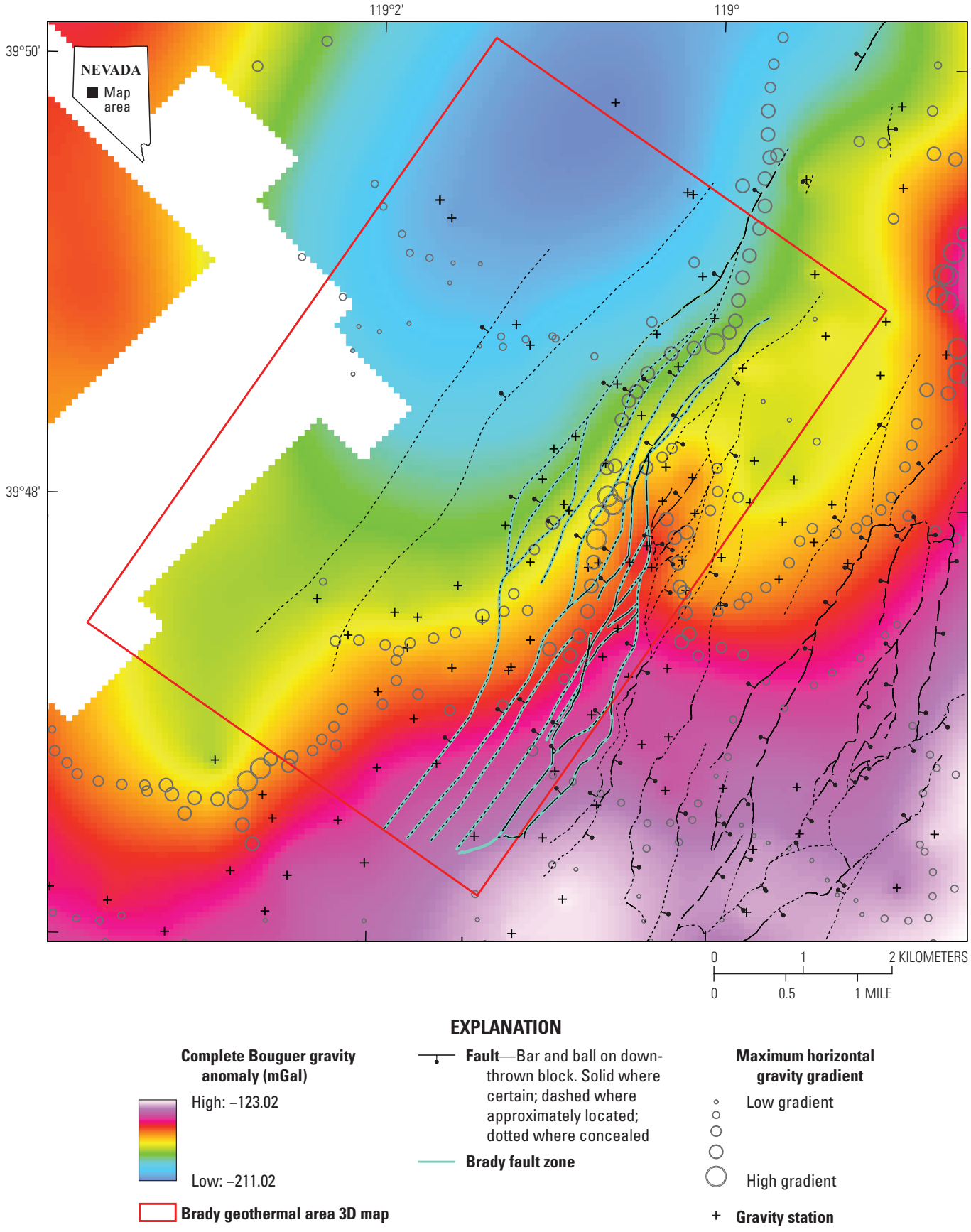

Figure 8. Map of complete Bouguer gravity anomaly (in milligals [mGal]) and the locations of the maximum horizontal gradients in the Bouguer gravity. Surface fault traces from Faulds and others (2017). Warm colors indicate high gravity; cool colors low gravity. 3D, three dimensional.

noted above, in areas of dense faulting and beneath the top of Miocene basaltic lavas (unit Tb), complex velocity structure and intricate impedance contrasts limit the coherence of the seismic reflection data, and thus our confidence in the interpretation. The structural and stratigraphic interpretations thus rely more on the downhole lithologic data, gravity data, geologic cross-section data, and projection of the geologic map data in these areas. The final fault profiles on the cross sections and fault surface traces on the map were digitized or digitally added to the 3D software environment.

The 3D stratigraphic contacts were constructed based on the bedrock exposures of Miocene volcanic and sedimentary rocks mapped in the study area by Faulds and others (2012, 2017) as well as by the four geologic cross sections constructed along with these published maps (Faulds and others, 2017). Downhole lithologic interpretation made from analyses of more than 19,000 m of well cuttings and cores from 21 wells provided additional constraints on the 3D lithologic geometries (fig. 5).

Three-dimensional fault and stratigraphic surfaces were built from the input data using a minimum tension gridding algorithm available within EarthVision software, which serves to generate relatively smooth surfaces while conforming to the input data (Dynamic Graphics Inc., 2018; Johnson and Taylor, 2010). In areas of sparse data, 3D fault and stratigraphic surfaces were manually adjusted to retain strike and dip of both faults and contacts as constrained by the input data, as well as unit thickness and trends in thickness change as constrained by input data (for example, Siler and Faulds, 2013; Siler and others, 2016a,b, 2019a,b). Data and metadata for the fault and stratigraphic surfaces are available for download at https://doi.org/10.3133/sim3469.

Upon completion of the 3D geologic map, 3D geophysical inversion modeling of gravity data was conducted to test whether the 3D lithologic framework is consistent with the observed gravity response across the entire volume (see Witter and others, 2016). The stratigraphic units from the 3D map were populated with measured and inferred values for rock density at the Brady geothermal area. This density model was inverted to produce a calculated gravity response, which was compared to the observed gravity. A low misfit between the calculated and observed gravity, that is, less than or equal to the gravity measurement error, was achieved. This suggests that the 3D geologic map is largely consistent with the observed gravity (Witter and others, 2016).

Stratigraphy of the 3D Geologic Map

The geologic units defined in the Brady geothermal area 3D geologic map are the units that may be reasonably mapped in three dimensions as constrained by the available data—that is, the geologic map data (fig. 2) and downhole lithologic data (fig. 5). In stratigraphically and structurally complex areas like the northern Hot Springs Mountains, it is generally necessary to lump many of the geologic units shown in 1:12,000- or 1:24,000-scale maps (for example, Faulds and others, 2012, 2017), rather than display them individually, because insufficient data are available to map many such units in the subsurface and thus in three dimensions. In the 3D map, the Holocene to Pleistocene geothermal features and deposits (unit Qg) are shown on the surface to convey the spatial distribution of these features, but unit Qg is not displayed in three dimensions since these are surficial or very shallow deposits. Non-geothermal Quaternary sediments and sedimentary rocks (units Qs and QTs) are distinguished based on whether they post-date shoreline features associated with the late Pleistocene middle Sehoo highstand of Lake Lahontan (Morrison, 1964, 1991; Adams and Wesnousky, 1998, 1999). Sedimentary deposits are lumped into unit Qs if they post-date the middle Sehoo shoreline features and unit QTs if they pre-date shoreline features, or if a relative age relation could not be determined.

The bedrock stratigraphy displayed in the 3D map follows the unit descriptions and relative age relations of Faulds and others (2017). This stratigraphy is supported by tephra chronology and $^{40}Ar/^{39}Ar$ dating from throughout the section. The reader is directed to the pamphlet accompanying Faulds and others (2017) for a description of these results. Underlying the geothermal deposits and geothermal features and Quaternary and Tertiary sedimentary rocks is a complex interfingering succession of late Miocene lacustrine sedimentary rocks, including limestone (unit Tls), and intercalated diatomaceous shale, siltstone, and limestone (unit Tsl). Unit Tsl is also interlayered throughout the underlying approximately 1,500-m-thick section dominated by late Miocene basaltic lavas (unit Tb). Unit Tb interfingers with late Miocene dacite lava flows and domes (unit Tpd), as well as late Miocene rhyolite and rhyodacite domes and flows (unit Tlr). The late Miocene volcanic and sedimentary rocks are underlain by early to middle Miocene dacite and andesite lavas (unit Tda) and locally by older lacustrine sedimentary rocks (unit Tslo), which are likely early Miocene based on stratigraphic position. Units Tda and Tslo are underlain by Oligocene to early Miocene rhyolite ash-flow tuffs (unit Trt), and undivided Mesozoic metamorphic and plutonic basement rocks (unit Mzu). More detailed descriptions of these units can be found in the Description of Map Units below.

Structure of the 3D Geologic Map

Faults in the 3D map are displayed as individual normal fault surfaces of infinitesimal thickness. In reality, faults occur as zones of fracturing, brecciation, and fault gouge of varying thickness (Cowie and Scholz, 1992; Scholz and others, 1993; Anders and Wiltschko, 1994). Although fractured areas that are meters to hundreds of meters thick may develop around faults, the thickness of these zones and any spatial changes in thickness cannot be quantified in the 3D map volume with the available data. As a result, the infinitesimal thickness is a necessary simplification regarding the location and geometry of faults.

All faults in the 3D map are displayed as normal faults. Faulting with components of dextral or sinistral shear occur within approximately 20 km of the 3D map. This suggests the possibility that some of the 3D mapped faults may have a component of lateral (dextral or sinistral) offset. None of the 3D

mapped faults, however, are shown with components of lateral offset in published 2D maps (Faulds and others, 2012, 2017), and fault kinematic data shown on the maps and published by Jolie and others (2015) supports this premise. This, along with a lack of any obvious lateral offset of geophysical anomalies, suggests that faults in the study area are predominantly normal faults, and therefore they are shown in the 3D map as such.

The 3D map displays an extensional syncline (for example, Faulds and Varga, 1998), with gently southeast-dipping strata at the northwest end of the map, transitioning to gently northwest-dipping strata to the southeast. The axis of the syncline is situated in the footwall of the north-northeast-striking Brady fault zone at the surface. The geologic contact between the base of the Cenozoic volcanic section (unit Tts at its base) and the Mesozoic crystalline basement (unit Mzu) along the northwest limb of the syncline dips approximately 20° southeast (~120° azimuth of dip direction), whereas the opposing limb of the syncline dips approximately 20° northwest (~300° azimuth of dip direction). Normal displacement across faults and tilting of the strata accommodates about 700 m of structural relief between the hinge zone and limbs of the syncline.

Thirty-two faults are defined within the 3D map. Faults generally strike north-northeast to northeast. Twenty-four faults dip steeply (~60°) northwest and seven faults dip steeply (~60°) southeast. The northwest dipping normal faults in the northwest part of the map (predominately the Brady fault zone) accommodate down dropping and southeast-ward tilting of the strata on the western limb of the extensional syncline. Of these faults, there are 20 individual fault strands that constitute the approximately 1-km-wide Brady fault zone. The Brady fault zone generally strikes about 030°, however, the central part of the 3D map is marked by an approximately 1-km-wide left stepover in the Brady fault zone. Fault segments and individual faults accommodating the stepover strike northerly, at an azimuth of about 000°.

3D Geologic Controls on Fracture Permeability and Fluid Flow

Faults commonly act as conduits for fluid flow in geothermal fields (Blackwell and others, 1999; Faulds and others, 2006, 2011). However, not all faults or sections of faults serve as fluid-flow conduits. Using the faults in the Brady 3D geologic map, we calculate the spatial distribution of four different structural characteristics that may control the distribution of flow pathways. The structural characteristics computed are the (1) slip tendency on faults, (2) dilation tendency on faults, (3) spatial density of faults, and (4) spatial density of fault intersections and fault terminations. Map sheet 2 shows the spatial relations between these four characteristics and the geothermal production wells at the Brady geothermal field at the two different reservoir production depths: 650 m depth (600 m elevation) and 1,700 m depth (−450 m elevation). In general, the geothermal production wells at the Brady geothermal field intersect faults with high slip and dilation tendency, high fault density, and high fault intersection or termination density.

Slip and Dilation Tendency

Faults and fractures that have a high resolved shear stress (that is, a high slip tendency) under modern stress conditions are likely to be critically stressed (that is, expected to slip given some cohesion and pore pressure) and conduct fluids relative to faults that have low shear stress (Barton and others, 1995; Zoback and Townend, 2001). Similarly, faults and fractures that have relatively low resolved normal stress (that is, a high dilation tendency) are expected to dilate and be associated with open fractures. Faults with high slip and (or) dilation tendency may constitute large volumes of connected fractures and a fluid flow system. We assume a normal faulting 3D stress model based on analysis of borehole breakouts in well 15-12 (fig. 4) with the minimum horizontal stress oriented along azimuth 097° (Jolie and others, 2015). Slip tendency, the ratio of the resolved shear stress on a fault (Morris and others, 1996), and dilation tendency, the ratio of resolved stresses acting normal to a fault (Ferrill and others, 1999), are calculated for each fault surface. Slip and dilation tendency values are shown on map sheet 2 along the 3D Brady fault zone with a 30 m buffer. The 30 m buffer distance was chosen for two reasons: (1) buffer widths smaller than about 30 m significantly lengthen software calculation time and require increasingly large and difficult-to-manage digital files and (2) the expected width of the damage zone of a 10-km-long fault zone with 100 m of displacement (the parameters of the Brady fault zone) is on the order of tens of meters (Scholz and others, 1993; Anders and Wiltschko, 1994). In reality, damage zone widths for faults with the general dimensions of the Brady fault zone range from 10 to 1,000 m and can vary significantly from fault to fault (Scholz and others 1993; Anders and Wiltschko, 1994). Ultimately, 30 m represents a reasonable approximation of the expected width of fault damage zones in the Brady geothermal area and is also feasible in terms of software and file size constraints.

Spatial Density of Faults and Fault Intersections and Terminations

Known faults are the best indicator of the locations where vertical fluid flow conduits may allow for upwelling of hot fluids from depth. Since spatial density of secondary fractures decreases with increasing distance from a fault (Cowie and Scholz, 1992; Scholz and others, 1993; Anders and Wiltschko, 1994), areas with a high spatial density of known faults are also likely to have a high overall density of fracturing and therefore may host fluid upwelling.

Tectonic stresses are concentrated at structural discontinuities like fault intersections and fault terminations (Pollard and Aydin, 1988; Scholz and others, 1993; Sibson, 1994; Peacock and Sanderson, 1991; Sanderson and Zhang, 2004; Fossen and Rotevatn, 2016; Siler and others, 2018). These locations are likely to host higher densities of secondary faults and fractures relative to areas distal to discontinuities. In the 3D map, the intersection lines between steeply dipping faults and the lines of termination of faults are manifest as steeply plunging zones of high facture density. These areas may represent

subvertical areas with high fracture density and (or) connectivity and serve as fluid flow conduits.

The spatial density of faults and fault intersections and terminations were calculated using a 3D kernel density function (for example, Alberti, 2011). The density function is calculated as the spatial density of uniform grids of vertices for fault planes, and uniform vertices along the lines of fault intersections and terminations. The results of the kernel density function are sensitive to three input parameters: (1) the distribution function used, (2) cell size, and (3) kernel bandwidth (that is, the search radius). Through several iterations it was decided using visual analysis that a normal distribution function, a cell size of 100 m, and a kernel bandwidth of 2 produced acceptable 3D density volumes that represented both individual faults and fault intersections and terminations, as well as the groupings of these features.

Data and metadata for the fault density, fault intersection and termination density, slip tendency, and dilation tendency volumes are available for download at https://doi.org/10.3133/sim3469.

Potential Applications of the 3D Map

Reservoir Modeling and Management

The 3D geologic map describes details of the structural and stratigraphic framework in the subsurface beneath the Brady geothermal area, an area that has been exploited for electricity generation since 1992 and direct uses of geothermal fluid (vegetable dehydration) since 1979 (Benoit and Butler, 1983). Generation of electricity from geothermal energy requires production and extraction of heat from hot fluid and (or) steam. Typically, the cooled fluid is subsequently re-injected back into the subsurface. Management of production and re-injection in a geothermal system is a complex balance of maintaining pressure in the geothermal reservoir through injection, while minimizing the temperature decline that can occur as a result of injection of the cooled fluid. Precise and accurate representations of geologic features can help to better constrain crucial parameters of numerical models of reservoirs, such as porosity and permeability, as well as the spatial distribution of these parameters.

Seismic Hazard Analysis

Western Nevada in the vicinity of the 3D map area has relatively high strain rates (Hammond and Thatcher, 2004; Kreemer and others, 2012, 2014) and thus is expected to host natural seismicity. Within the 3D map, at least one relatively recent slip event has been documented by paleoseismic trenching, a 2-m-high scarp in alluvium that is younger than the approximately 15.5 ka Lake Lahontan highstand (Wesnousky and others, 2005). Surface cracks in Holocene sedimentary deposits and silicified Holocene alluvium suggest that the Brady fault zone has remained active into the Holocene (Faulds and others, 2017). The 3D geologic map provides data on many key characteristics of the faults within the map area, including fault orientations, fault lengths, fault offsets, and the spatial distribution of faults. This information can be paired with local seismological data and the location of sensitive infrastructure—for example, the geothermal power station and vegetable dehydration facility—to evaluate the hazard and risk associated with natural seismicity (for example, Kaven and others, 2019).

Conventional Geothermal and Enhanced Geothermal System Exploration and Research

Renewable electricity generation from conventional geothermal systems and enhanced geothermal systems (EGS), has the potential to constitute a significant portion of future electricity needs for the United States (Tester and others, 2006; Blackwell and others, 2007; Williams and others, 2008, 2009). Power production from conventional geothermal systems relies on generation of electricity from naturally occurring subsurface steam or hot water. EGS relies on generation of permeability in hot but impermeable rock through a variety of subsurface engineering processes. The goal is to produce an exploitable fluid circulation system between a group of wells or to link newly generated permeability to an existing developed geothermal field (near-field EGS) (Tester and others, 2006). 3D structural and geologic information is critically important for EGS research and exploration (for example, Siler and others, 2019a). A successful near-field EGS development has occurred at Desert Peak (fig. 1; Rose and others, 2012), about 10 km southeast of the Brady area, and an EGS project was conducted at the Brady geothermal field beginning in 2008 (Lu, 2018).

Conventional geothermal systems in the western United States, including Brady, typically occur at discontinuities along faults (Curewitz and Karson, 1997; Faulds and others, 2006, 2011). These areas have inherent structural complexity exemplified by a high local density of interconnected faults and fractures. Relatively high temperatures in the subsurface drive hydrothermal circulation through these permeable pathways. Where fluids are hot enough and permeability is high enough, electricity can be generated. Western Nevada proximal to the northern Hot Springs Mountains hosts 13 known geothermal systems. Seven of these, including the Brady geothermal area, have been developed for electricity production (fig. 1; Faulds and others, 2006, 2011; Faulds and Hinz, 2015). Stepovers in normal fault systems, like that at Brady, are one type of structural discontinuity that hosts many geothermal systems that have been developed for electricity production and many more known, but as yet undeveloped, systems (Faulds and others, 2013). Additional but thus far undiscovered geothermal systems may reside at similar fault stepovers throughout the western United States and worldwide. The 3D map provides a detailed representation of the subsurface architecture of faults within the stepover. This provides the context for understanding the geologic and tectonic factors that control permeability generation and geothermal fluid flow in this setting and in analogous settings.

Education and Scientific Inquiry

A 3D geologic map supplements the information provided in 2D geologic maps by allowing the user to visualize complex geologic features in three dimensions. Geologic features may be viewed from different angles, and slices through the map can illustrate geologic relations along cross sections of any orientation. The complex, 3D spatial relations generated by faulting, folding, erosion, sedimentation, and other geologic processes may be visualized relatively quickly and easily, making 3D geologic maps useful interpretive tools and teaching aids. This 3D map may be used by the academic community and by the public to visualize the subsurface geologic relations present in the Brady geothermal area.

Basin Hydrogeology

Shallow groundwater resources associated with both agricultural irrigation and drinking water are critical to the sustainability of many public and governmental interests in arid parts of the western United States, including the Basin and Range region. Within geothermal fields, high temperatures, salinity, or water chemistry make hydrothermal fluids from deeper geothermal reservoirs unsuitable for these purposes. In addition to characterizing the hydrothermal system, the 3D geologic map provides information that is applicable to the assessment and management of the water systems that are distinct from the hydrothermal system. Both sedimentary and volcanic rocks can host important shallow aquifers (for example, Glancy, 1986; Maurer and Welch, 2001). Faults and basin structure, which are shown in the map, significantly influence the distribution of sedimentary and volcanic rocks. The local tectonic setting affects the processes that control sediment distribution, composition, deposition, grain size distribution, and, therefore, physical properties like porosity and permeability related to groundwater storage and transport. Local tectonics also influence the locations, facies, and aquifer potential of volcanic rocks. By providing a 3D perspective on the stratigraphic and structural framework, the 3D map can be used to study both shallow groundwater aquifers and deeper geothermal reservoirs and, thus, the overall hydrogeology of the basin.

Acknowledgments

This research was supported by the U.S. Department of Energy (awards DE-FG36-02ID14311 and DE-FG36-08GO18200), Ormat Technologies, Inc., the U.S. Geological Survey STATEMAP Program (agreement no. G11AC20244 to J.E. Faulds), and an American Recovery and Reinvestment Act grant from the U.S. Department of Energy (agreement no. EE0002748 to J.E. Faulds). We thank Lowell Price at the Nevada Division of Minerals for his help obtaining some of the data used in this study. Funds associated with the Geothermal Resources Investigations Project (GRIP) and Mendenhall Program at the U.S. Geologic Survey also supported this project.

DESCRIPTION OF MAP UNITS

GEOTHERMAL DEPOSITS

Qg **Geothermal deposits and geothermal features (Holocene to late Pleistocene)**—Silicified mud, silicified sand, silicified colluvium, hydrothermal craters, fumaroles, and thermal ground. This is a lumped unit consisting of units Qsc, Qss, Qsim, Qssi, Qsio, and geothermal features from Faulds and others (2017). These units are shown at the surface in the 3D map, but they are surficial or near-surface units and features, so they are not displayed with any depth extent in the 3D map

SEDIMENTARY DEPOSITS

Qs **Surficial sediments and sedimentary rocks (Holocene to late Pleistocene)**—Alluvial, alluvial fan, playa, sand dune, colluvial, and eolian sand deposits. This is a lumped unit consisting of units Qa, Qfy1, Qfy2, Qp, Qd, Qe, and Qc from Faulds and others (2017). Represents sedimentary units that post-date the middle Sehoo (approximately 13–14 ka) highstand of Lake Lahontan, which is late Pleistocene (Morrison, 1964, 1991; Adams and Wesnousky, 1998, 1999). This unit is less than 10 m thick

QTs **Sedimentary rocks (late Pleistocene to late Miocene)**—Alluvium, lacustrine deposits, beach deposits, silt, tufa, shoreline tufa deposits, basin-fill sediments, and tuffaceous sediments. This is a lumped unit consisting of units QTa, Qsm, Qsmb, Qsms, Qsmt, Qtus, Qfi, Qfo, and Qsl from Faulds and others (2017). Represents sedimentary units

that pre-date the middle Sehoo highstand of Lake Lohantan, which is late Pleistocene (Morrison, 1964, 1991; Adams and Wesnousky, 1998, 1999) or units for which a relative age determination relative to the middle Sehoo highstand of Lake Lahontan could not be made

Tsy **Basin-fill sediments (late Miocene)**—Fine-grained basin fill sediments. This unit is not exposed at the surface but interpreted from seismic reflection data (fig. 7) as closely spaced, continuous reflectors. This is a lumped unit consisting of units Tts and Tsy from Faulds and others (2017)

BEDROCK

SEDIMENTARY AND VOLCANIC ROCKS

Tsl **Lacustrine sedimentary rocks (late Miocene)**—Lacustrine sedimentary rocks including sandstone, siltstone, silicified siltstone, diatomaceous shale, tuffaceous siltstone, and minor interbedded limestone. This is a lumped unit consisting of units Tsl, Tds, Tsso, Tws, and Tsls from Faulds and others (2017). As thick as ~160 m locally, but more commonly continuous sections are 20–60 m thick. Interlayered with units Tls, Tpd, Tlr, and Tb throughout the section

Tls **Limestone (late Miocene)**—Lacustrine limestone from Faulds and others (2017). Abundant coquinas of ostracod shells. As thick as 150 m locally, but more commonly continuous sections are 20–50 m thick. Intercalated with units Tsl and Tb throughout the section

Tb **Basaltic lavas (late Miocene)**—Dominated by aphanitic basaltic lavas, but including minor basaltic flow breccia, basaltic andesite lavas, andesite lavas, dacite lavas, basaltic sandstone, basaltic intrusions, basaltic andesite intrusions, altered basaltic lavas, and older diatomaceous shale. This is a lumped unit consisting of units Tab, Tb, Tbb, Tbi, Tbai, Tds, Tdso, Tbs, Tbo, and Tabo from Faulds and others (2017). As thick as ~800 m, but more commonly continuous sections are 200–500 m thick. Interlayered with units Tls, Tsl, Tpd, and Tlr throughout the section

Tpd **Dacite lavas and domes (late Miocene)**—Discontinuous unit of porphyritic dacite lava flows and domes from Faulds and others (2017). Not exposed at the surface in the 3D map or that of Faulds and others (2017) but identified between about 170 and 600 m depth in nine bore holes in the central part of the 3D map. 100–200 m thick where observed in wells. Interlayered with unit Tb

Tlr **Rhyolite to rhyodacite lavas and domes (late Miocene)**—Discontinuous unit of rhyolite to rhyodacite lavas and domes from Faulds and others (2017). Not exposed at the surface in the 3D map or that of Faulds and others (2017). Identified between approximately 400 and 750 m depth in five boreholes. Represented as northwest trending approximately 20-m-thick flow lobes in the 3D map. Interlayered with unit Tb near the base of unit Tb or stratigraphically beneath Tb

Tda **Dacite and andesite lavas (early to middle Miocene)**—Undivided dacite and andesite lavas from Faulds and others (2017). Not exposed at the surface in the 3D map or that of Faulds and others (2017). Exposed approximately 7 km east-northeast of the 3D map on the eastern part of the northern Hot Springs Mountains in the Desert Peak quadrangle (fig. 2; Faulds and others, 2012). Identified in wells BCH-2 and BCH-3 as approximately 250- to 400-m-thick continuous sections and as two <40 m thick sections in well 27-1. Interlayered with unit Tb in wells BCH-2 and 27-1 and underlies unit Tb in BCH-3. Shown as stratigraphically beneath unit Tb in the 3D map

Tslo **Older lacustrine sedimentary rocks (early Miocene)**—Discontinuous section of lacustrine sedimentary rocks occurring in the central part of the 3D map area. Not exposed at the surface in the 3D map or that of Faulds and others (2017). An approximately 80-m-thick section occurs in well BCH-2 at about 1,100 m depth, which is inferred to be a local sedimentary basin

Trt **Rhyolite ash-flow tuffs (Oligocene to early Miocene)**—Undivided rhyolite ash-flow tuffs from Faulds and others (2017). Not exposed at the surface in the 3D map or that of Faulds and others (2017). Identified in five wells in the 3D map. The basal contact is identified in wells BCH-3, 82A-11, and 27-1, constraining the thickness to 150–400 m

CRYSTALINE BASEMENT ROCKS

Mzu **Metamorphic and plutonic rocks (Mesozoic)**—Undivided metavolcanics, metasedimentary (Lutz and others, 2011; and cuttings, core, and thin section analyses in this study), and possibly plutonic basement rocks. Not exposed at the surface in the 3D map or that of Faulds and others (2017). Exposed approximately 5 km east-northeast of the 3D map on the eastern side of the northern Hot Springs Mountains in the Desert Peak quadrangle (Faulds and others, 2012), where the Mesozoic basement consists of Jurassic diorite plutons (units Jd and Jda) and Jurassic or Triassic quartzite, conglomerate, limestone, siltite (unit JTrms), altered andesite lavas (unit JTrma), and undivided metamorphic rocks (unit JTrmu). These are probably correlative to similar basement lithologies of similar age identified at depth about 45 km to the southeast of the 3D map area in the southern Carson Sink (Siler and others, 2019a)

References Cited

Adams, K.D., and Wesnousky, S.G., 1998, Shoreline processes and the age of the Lake Lahontan highstand in the Jessup embayment, Nevada: Geological Society of America Bulletin, v. 110, no. 10, p. 1,318–1,332.

Adams, K.D., and Wesnousky, S.G., 1999, The Lake Lahontan highstand—Age, surficial characteristics, soil development, and regional shoreline correlation: Geomorphology, v. 30, no. 4, p. 357–392.

Alberti, M., 2011, 3D point cloud density calculation—A C++ program: GISoftware blog, May 6, 2011, accessed April 30, 2020, at https://gisoftw.blogspot.com/2011/05/3d-point-density-calculation-c-program.html.

Ali, S.T., Akerley, J., Baluyut, E.C., Cardiff, M., Davatzes, N.C., Feigl, K.L., Foxall, W., Fratta, D., Mellors, R.J., Spielman, P., and Wang, H.F., 2016, Time-series analysis of surface deformation at Brady Hot Springs geothermal field (Nevada) using interferometric synthetic aperture radar: Geothermics, v. 61, p. 114–120, accessed March 19, 2020, at https://doi.org/10.1016/j.geothermics.2016.01.008.

Anders, M.H., and Wiltschko, D.V., 1994, Microfracturing, paleostress and the growth of faults: Journal of Structural Geology, v. 16, p. 795–815, accessed July 1, 2016, at https://doi.org/10.1016/0191-8141(94)90146-5.

Barton, C.A., Zoback, M.D., and Moos, D., 1995, Fluid flow along potentially active faults in crystalline rock: Geology, v. 23, no. 8, p. 683–686, accessed March 2, 2020, at https://doi.org/10.1130/0091-7613(1995)023%3C0683:FFAPAF%3E2.3.CO;2.

Benoit, W.R., and Butler, R.W., 1983, A review of high-temperature geothermal developments in the northern Basin and Range Province: Geothermal Resources Council Special Report no. 13, p. 57–80.

Benoit, W.R., Hiner, J.E., and Forest, R.T., 1982, Discovery and geology of the Desert Peak geothermal field—A case history: Nevada Bureau of Mines and Geology Bulletin 97, 82 p.

Blackwell, D.D., Negraru, P.T., and Richards, M.C., 2007, Assessment of the enhanced geothermal system resource base of the United States: Natural Resources Research, v. 15, p. 283–308, accessed August 4, 2016, at https://doi.org/10.1007/s11053-007-9028-7.

Blackwell, D.D., Wisian, K.W., Benoit, D., and Gollan, B., 1999, The structure of a "typical" Basin and Range geothermal system, from thermal and gravity data: Geothermal Resources Council Transactions, v. 23, p. 525–531.

Blakely, R.J., 1995, Potential theory in gravity and magnetic applications: Cambridge University Press, 441 p.

Cardiff, M., Lim, D.D., Patterson, J.R., Akerley, J., Spielman, P., Lopeman, J., Walsh, P., Singh, A., Foxall, W., Wang, H.F., and Lord, N.E., 2018, Geothermal production and reduced seismicity—Correlation and proposed mechanism: Earth and Planetary Science Letters, v. 482, p. 470–477 accessed March 19, 2020, at https://doi.org/10.1016/j.epsl.2017.11.037.

Cashman, P.H., and Fontaine, S.A., 2000, Strain partitioning in the northern Walker Lane, western Nevada and northeastern California: Tectonophysics, v. 326, p. 111–130.

Colgan, J.P., Dumitru, T.A., Reiners, P.W., Wooden, J.L., and Miller, E.L., 2006, Cenozoic tectonic evolution of the Basin and Range Province in northwestern Nevada: American Journal of Science, v. 306, p. 616–654, accessed June 1, 2016, at https://doi.org/10.2475/08.2006.02.

Cousens, B.L., Prytulak, J., Henry, C.D., Alcazar, A., and Brownrigg, T., 2008, The geology, geochronology and geochemistry of the Miocene–Pliocene ancestral Cascades Arc, northern Sierra Nevada, California/Nevada—The roles of the upper mantle, subducting slab, and the Sierra Nevada lithosphere: Geosphere, v. 4, p. 829–853.

Cowie, P.A., and Scholz, C.H., 1992, Displacement-length scaling relationship for faults; data synthesis and discussion: Journal of Structural Geology, v. 14, no. 10, p. 1,149–1,156.

Crafford, A.E.J., 2007, Geologic map of Nevada: U.S. Geological Survey Data Series 249, 1 CD-ROM, 46 p., 1 plate.

Crafford, A.E.J., 2010, Geologic terrane map of Nevada: Nevada Bureau of Mines and Geology Open-File Report OF104, 1 CD-ROM, 46 p., 2 plates.

Curewitz, D., and Karson, J.A., 1997, Structural settings of hydrothermal outflow—Fracture permeability maintained by fault propagation and interaction: Journal of Volcanology and Geothermal Research, v. 79, p. 149–168, accessed July 1, 2016, at https://doi.org/10.1016/S0377-0273(97)00027-9.

Dynamic Graphics, Inc., 2018, EarthVision reference manual v. 10: Alameda, Calif., Dynamic Graphics, Inc., 2,387 p.

Faulds, J.E., Coolbaugh, M.F., Benoit, D., Oppliger, G., Perkins, M., Moeck, I., and Drakos, P., 2010a, Structural controls of geothermal activity in the northern Hot Springs Mountains, western Nevada—The tale of three geothermal systems (Brady's, Desert Perk, and Desert Queen): Geothermal Resources Council Transactions, v. 34, p. 675–683.

Faulds, J.E., Coolbaugh, M.F., Vice, G.S., and Edwards, M.L., 2006, Characterizing structural controls of geothermal fields in the northwestern Great Basin—A progress report: Geothermal Resources Council Transactions, v. 30, p. 69–76.

Faulds, J.E., Garside, L.J., and Oppliger, G., 2003, Structural analysis of the Desert Peak–Brady geothermal fields, northwest Nevada—Implications for understanding links between northeast-trending structures and geothermal reservoirs in the Humboldt structural zone: Geothermal Resources Council Transactions, v. 27, p. 859–864.

Faulds, J.E., Henry, C.D. and Hinz, N.H., 2005, Kinematics of the northern Walker Lane—An incipient transform fault along the Pacific–North American plate boundary: Geology, v. 33, no. 6, p. 505–508, accessed June 25, 2020, at https://doi.org/10.1130/G21274.1.

Faulds, J.E., and Hinz, N.H., 2015, Favorable tectonic and structural settings of geothermal systems in the Great Basin region, western USA—Proxies for discovering blind geothermal systems: Proceedings, World Geothermal Congress, Melbourne, Australia, 19–25 April, p. 1–6.

Faulds, J.E., Hinz, N.H., Coolbaugh, M.F., Cashman, P.H., Kratt, C., Dering, G.M., Edwards, J., Mayhew, B., and Mclachlan, H., 2011, Assessment of Favorable structural settings of geothermal systems in the Great Basin, Western USA: Geothermal Resources Council Transactions v. 35, p. 777–784.

Faulds, J.E., Hinz, N.H., Dering, G.M., and Siler, D.L., 2013, The hybrid model—The most accommodating structural setting for geothermal power generation in the Great Basin, western USA: Geothermal Resources Council Transactions, v. 37, p. 4–10.

Faulds, J.E., Moeck, I., Drakos, P., and Zemach, E., 2010b, Structural assessment and 3-D geological modeling of the Brady's geothermal area, Churchill County (Nevada, USA)—A preliminary report: Proceedings, Thirty-Fifth Workshop on Geothermal Reservoir Engineering, Stanford University, February 1–3, SGP-TR-188, p. 1–5.

Faulds, J.E., Ramelli, A.R., Coolbaugh, M.F., Hinz, N.H., Garside, L.J., and Queen, J.H., 2017, Preliminary geologic map of the Bradys geothermal area, Churchill County, Nevada: Nevada Bureau of Mines and Geology Open-File Report 17-4, scale 1:12,000, 6 p.

Faulds, J.E., Ramelli, A.R., Garside, L.J., Coolbaugh, M.F., and Green, H.F., 2012, Preliminary geologic map of the Desert Peak quadrangle, Churchill County, Nevada: Nevada Bureau of Mines and Geology Open-File Report OF-12-5, 1:24,000 scale, 1 sheet.

Faulds, J.E., and Varga, R., 1998, The role of accommodation zones and transfer zones in the regional segmentation of extended terranes: Geological Society of America Special Paper 323, p. 1–46.

Ferrill, D.A., Winterle, J., Wittmeyer, G., Sims, D., Colton, S., Armstrong, A., Horowitz, A.S., Meyers, W.B., and Simons, F.F., 1999, Stressed rock strains groundwater at Yucca Mountain, Nevada: GSA Today, v. 9, p. 1–8.

Fosdick, J.C., and Colgan, J.P., 2008, Miocene extension in the East Range, Nevada—A two-stage history of normal faulting in the northern Basin and Range: Geosphere, v. 120, no. 9/10, p. 1,198–1,213.

Fossen, H., and Rotevatn, A., 2016, Fault linkage and relay structures in extensional settings—A review: Earth Science Reviews, v. 154, p. 14–28.

Glancy, P.A., 1986, Geohydrology of the basalt and unconsolidated sedimentary aquifers in the Fallon area, Churchill County, Nevada: U.S. Geological Survey Water-Supply Paper 2263, 70 p.

Hammond, W.C., and Thatcher, W., 2004, Contemporary tectonic deformation of the Basin and Range province, western United States—10 years of observation with the Global Positioning System: Journal of Geophysical Research, v. 109, no. B8403, accessed March 2, 2020, at https://doi.org/10.1029/2003JB002746.

Henry, C.D., 2008, Ash-flow tuffs and paleovalleys in northeastern Nevada—Implications for Eocene paleogeography and extension in the Sevier hinterland, northern Great Basin: Geosphere, v. 4, no. 1, p. 1–35, accessed September 1, 2016, at https://doi.org/10.1130/GES00122.1.

Henry, C.D., Hinz, N.H., Faulds, J.E., Colgan, J.P., John, D.A., Brooks, E.R., Cassel, E.J., Garside, L.J., Davis, D.A., and Castor, S.B., 2012, Eocene–early Miocene paleotopography of the Sierra Nevada-Great Basin-Nevadaplano based on widespread ash-flow tuffs and paleovalleys: Geosphere, v. 8, no. 1, p. 1–27, accessed July 1, 2016, at https://doi.org/10.1130/GES00727.1.

Hinz, N.H., Faulds, J.E., and Siler, D.L., 2013, Developing systematic workflow from field work to quantitative 3-D modeling for successful exploration of structurally controlled geothermal systems: Geothermal Resources Council Transactions, v. 37, p. 275–279.

Johnson, C.A., and Taylor, C.D., 2010, Three-dimensional modeling and visualization of Greens Creek drill-hole data, *in* Taylor, C.D., and Johnson, C.A., eds., Geology, geochemistry, and genesis of the Greens Creek massive sulfide deposit, Admiralty Island, southeastern Alaska: U.S. Geological Survey Professional Paper 1763, 429 p., 7 plates on CD.

Jolie, E., Faulds, J.E., and Moeck, I., 2012, The development of a 3-D structural-geological model as part of the geothermal exploration strategy—A case study from the Brady's geothermal system, Nevada, USA: Proceedings, Thirty-Seventh Workshop on Geothermal Reservoir Engineering, Stanford University, p. 421–425.

Jolie, E., Moeck, I., and Faulds, J.E., 2015, Quantitative structural-geological exploration of fault-controlled geothermal systems—A case study from the Basin-and-Range Province, Nevada (USA): Geothermics, v. 54, p. 54–67, accessed June 1, 2016, at https://doi.org/10.1016/j.geothermics.2014.10.003.

Kaven, J.O., Majer, E.L., Foxall, W., Sonnenthal, E.L., and Pettitt, W., 2019, Seismic hazard assessment at the Fallon, Nevada, Frontier Observatory for Research in Geothermal Energy site: U.S. Geological Survey Open-File Report 2019–1020, 16 p., accessed November 7, 2019, at https://doi.org/10.3133/ofr20191020.

Kratt, C., Calvin, W., and Coolbaugh, M., 2006, Geothermal exploration with Hymap hyperspectral data at Brady–Desert Peak, Nevada: Remote Sensing of the Environment, v. 104, no. 3, p. 313–324, accessed March 19, 2020, at https://doi.org/10.1016/j.rse.2006.05.005.

Kreemer, C., Blewitt, G., and Klein, E.C., 2014, A geodetic plate motion and global strain rate model: Geochemistry, Geophysics, Geosystems, v. 15, p. 3,849–3,889, accessed November 4, 2016, at https://doi.org/10.1002/2014GC005407.

Kreemer, C., Hammond, W.C., Blewitt, G., Holland, A.A., and Bennett, R.A., 2012, A geodetic strain rate model for the Pacific-North American plate boundary, western USA: Nevada Bureau of Mines and Geology Map 178, scale 1:1.500,000, 1 sheet.

Li, Z., and Zhan, Z., 2018, Pushing the limit of earthquake detection with distributed acoustic sensing and template matching—A case study at the Brady geothermal field: Geophysical Journal International, v. 215, no. 3, p. 1,583–1,593, accessed March 19, 2020, at https://doi.org/10.1093/gji/ggy359.

Lu, S-M., 2018, A global review of enhanced geothermal system (EGS): Renewable and Sustainable Energy Reviews, v. 81, no. 2, p. 2,902–2,921.

Lutz, S.J., Zutshi, A., Robertson-Tait, A., Drakos, P., and Zemach, E., 2011, Lithologies, hydrothermal alteration, and rock mechanical properties in wells 15-12 and BCH-3, Bradys hot springs geothermal field, Nevada: Geothermal Resources Council Transactions, v. 35, p. 469–476.

Maurer, D.K., and Welch, A.H., 2001, Hydrogeology and geochemistry of the Fallon basalt and adjacent aquifers, and potential sources of basalt recharge, in Churchill County, Nevada: U.S. Geological Survey Water-Resources Investigations Report 01-4130, 2 sheets, 72 p.

Moeck, I., Hinz, N.H., Faulds, J.E., Bell, J.W., Kell-Hills, A., and Louie, J., 2010, 3-D geological mapping as a new method in geothermal exploration—A case study from central Nevada: Geothermal Resources Council Transactions, v. 34, p. 807–812.

Morris, A., Ferrill, D.A., and Henderson, D.B., 1996, Slip-tendency analysis and fault reactivation: Geology, v. 24, p. 275–278.

Morrison, R.B., 1964, Lake Lahontan—Geology of Southern Carson Desert, Nevada: U.S. Geological Survey Professional Paper 401, plates 3 and 5.

Morrison, R.B., ed., 1991, Quaternary nonglacial geology—Conterminous US: Geological Society of America, v. K–2, variously paged.

Oldow, J.S., 1984, Evolution of a late Mesozoic back-arc fold and thrust belt, northwestern Great Basin, U.S.A.: Tectonophysics, v. 102, no. 1–4, p. 245–274.

Parker, L.M., Thurber, C.H., Zeng, X., Li, P., Lord, N.E., Fratta, D., Wang, H.F., Robertson, M.C., Thomas, A.M., Karplus, M.S., and Nayak, A., 2018, Active-source seismic tomography at the Brady geothermal field, Nevada, with dense nodal and fiber-optic seismic arrays: Seismological Research Letters, v. 89, no. 5, p. 1,629–1,640, accessed March 19, 2020, at https://doi.org/10.1785/0220180085.

Patterson, J.R., Cardiff, M., Coleman, T., Wang, H., Feigl, K.L., Akerley, J., and Spielman, P., 2017, Geothermal reservoir characterization using distributed temperature sensing at Brady Geothermal Field, Nevada: The Leading Edge, v. 36, p. 1024a1–1024a7, accessed March 19, 2020, at https://doi.org/10.1190/tle36121024a1.1.

Peacock, D.C.P., and Sanderson, D.J., 1991, Displacements, segment linkage and relay ramps in normal fault zones: Journal of Structural Geology, v. 13, no. 6, p. 721–733, accessed March 2, 2020, at https://doi.org/10.1016/0191-8141(91)90033-F.

Pollard, D.D., and Aydin, A., 1988, Progress in understanding jointing over the past century: Geologic Society of America Bulletin, v. 100, p. 1,181–1,204, accessed March 2, 2020, at https://doi.org/10.1130/0016-7606(1988)100%3C1181:PIUJOT%3E2.3.CO;2.

Queen, J.H., Daley, T.M., Majer, E.L., Nihei, K.T., Siler, D.L., and Faulds, J.E., 2016, Surface reflection seismic and vertical seismic profile at Brady's Hot Springs, NV, USA: Proceedings, 41st Workshop on Geothermal Reservoir Engineering, Stanford University, 14 p.

Reinisch, E.C., Cardiff, M., and Feigl, K.L., 2018, Characterizing volumetric strain at Brady Hot Springs, Nevada, USA using geodetic data, numerical models and prior information: Geophysical Journal International, no. 215(2), p. 1,501–1,513, accessed March 19, 2020, at https://doi.org/10.1093/gji/ggy347.

Rose, P., Hickman, S., Moore J., Kovac, K., Adams, M., Mella, M., Wannamaker, P., Julian, B., Foulger, G., Swenson, D., Gosavi, S., Bhat, A., Richards-Dinger, K., Monastero, F., Weidler, R., Baisch, S., Ghassemi, A., and Megel, T., 2012, Final Report—Creation of an Enhanced Geothermal System through Hydraulic and Thermal Stimulation: U.S. Department of Energy, Geothermal Technologies Program [contract DE-FC07-01ID14186], 484 p.

Sanderson, D.J., and Zhang, X., 2004, Stress-controlled localization of deformation and fluid flow in fractured rocks: Geological Society of London Special Publications, v. 231, p. 299–314, accessed March 3, 2020, at http://dx.doi.org/10.1144/GSL.SP.2004.231.01.18.

Scholz, C.H., Dawers, N.H., Yu, J., Anders, M.H., and Cowie, P.A., 1993, Fault growth and fault scaling laws—Preliminary results: Journal of Geophysical Research, v. 98, p. 951–961.

Schweickert, R.A., and Cowan, D.S., 1975, Early Mesozoic tectonic evolution of the western Sierra Nevada, California: Geological Society of America Bulletin, v. 86, p. 1,329–1,336.

Sibson, R.H., 1994, Crustal stress, faulting and fluid flow, *in* Parnell, J., ed., Geofluids—Origin, migration and evolution of fluids in sedimentary basins: Geological Society of London Special Publications, p. 69–84.

Siler, D.L., and Faulds, J.E., 2013, Three-dimensional geothermal fairway mapping—Examples from the western Great Basin, USA: Geothermal Resources Council Transactions, v. 37, p. 327–332.

Siler, D.L., Faulds, J.E., Glen, J.M.G., Hinz, N.H., Witter, J.B., Blake, K., Queen, J., and Fortuna, M., 2019a, Three-dimensional geologic map of the southern Carson Sink, Nevada, including the Fallon FORGE area: U.S. Geological Survey Scientific Investigations Map 3437, pamphlet 22 p., accessed November 7, 2019, at https://doi.org/10.3133/sim3437.

Siler, D.L., Faulds, J.E., Hinz, N.H., Dering, G.M., Edwards, J.H., and Mayhew, B.M., 2019b, Three-dimensional geologic mapping to assess geothermal potential—Examples from Nevada and Oregon: Geothermal Energy, v. 7, no. 2, accessed October 1, 2019, at https://doi.org/10.1186/s40517-018-0117-0.

Siler, D.L., Faulds, J.E., Mayhew, B., and McNamara, D.D., 2016a, Analysis of the favorability for geothermal fluid flow in 3-D; Astor Pass geothermal prospect, Great Basin, northwestern Nevada, USA: Geothermics, v. 60, p. 1–12, accessed May 1, 2016, at https://doi.org/10.1016/j.geothermics.2015.11.002.

Siler, D.L., Hinz, N.H., and Faulds, J.E., 2018, Stress concentrations at structural discontinuities in active fault zones in the western United States—Implications for permeability and fluid flow in geothermal fields: Geological Society of America Bulletin, v. 130, p. 1,273–1,288, accessed May 1, 2020, at https://doi.org/10.1130/B31729.1.

Siler, D.L., Hinz, N.H., Faulds, J.E., and Queen, J., 2016b, 3-D analysis of geothermal fluid flow favorability—Brady's, Nevada, USA: Proceedings, 41st Workshop on Geothermal Reservoir Engineering, Stanford University, p. 1–10.

Stewart, J.H., and Carlson, J.E., 1978, Geologic map of Nevada: U.S. Geological Survey Miscellaneous Field Studies Map MF–930, 1:500,000 scale, 1 sheet.

Stockli, D.F., Surpless, B.E., Dumitru, T.A., and Farley, K.A., 2002, Thermochronological constraints on the timing and magnitude of Miocene and Pliocene extension in the central Wassuk Range, western Nevada: Tectonics, v. 21, no. 4, p. 1–21, accessed August 1, 2016, at https://doi.org/10.1029/2001TC001295.

Tester, J.W., Anderson, B.J., Batchelor, A.S., Blackwell, D.D., DiPippo, R., Drake, E.M., Garnish, J., Livesay, B., Moore, M.C., Nichols, K., Petty, S., Toksöv, M.N., Veatch, R.W.J., Baria, R., Augustine, C., Murphy, E., Negraru, P., and Richards, M., 2006, The future of geothermal energy—Impact of enhanced geothermal systems (EGS) on the United States in the 21st century: Massachusetts Institute of Technology, no. 209, 372 p.

U.S. Geological Survey, 2006, Quaternary fault and fold database of the United States: U.S. Geological Survey website, accessed February 11, 2021, at https://www.usgs.gov/natural-hazards/earthquake-hazards/faults?qt-science_support_page_related_con=4#qt-science_support_page_related_con.

Wernicke, B.P., England, P.C., Sonder, L.J., and Christiansen, R.L., 1987, Tectonomagmatic evolution of Cenozoic extension in the North American Cordillera: The Geological Society of London Special Publications, v. 28, p. 203–221, accessed October 1, 2019, at https://doi.org/10.1144/GSL.SP.1987.028.01.15.

Wesnousky, S.G., Barron, A.D., Briggs, R.W., Caskey, S.J., Kumar, S., and Owen, L., 2005, Paleoseismic transect across the northern Great Basin: Journal of Geophysical Research, v. 110, no. B05408, p. 1–25, accessed August 20, 2019, at https://doi.org/10.1029/2004JB003283.

Williams, C.F., Reed, M.J., Mariner, R.H., DeAngelo, J., and Galanis, S.P.J., 2008, Assessment of moderate- and high-temperature geothermal resources of the United States: U.S. Geological Survey Fact Sheet 2008-3082, 4 p.

Williams, C.F., Reed, M.J., Mariner, R.H., DeAngelo, J., and Galanis, S.P.J., 2009, Quantifying the undiscovered geothermal resources of the United States: Geothermal Resources Council Transactions, v. 33, p. 1–8.

Witter, J.B., Siler, D.L., Faulds, J.E., and Hinz, N.H., 2016, 3D geophysical inversion modeling of gravity data to test the 3D geologic model of the Bradys geothermal area, Nevada, USA: Geothermal Energy, v. 4, no. 14, p. 1–22, accessed November 6, 2016, at https://doi.org/10.1186/s40517-016-0056-6.

Zoback, M.D., and Townend, J., 2001, Implications of hydrostatic pore pressures and high crustal strength for the deformation of intraplate lithosphere: Tectonophysics, v. 336, p. 19–30, accessed March 2, 2020, at https://doi.org/10.1016/S0040-1951(01)00091-9.